Automated Feature-based Alignment for 3D Volume Reconstruction of CLSM Imagery

Sang-Chul Lee and Peter Bajcsy[*]

1008 National Center for Supercomputing Applications, 1205 W. Clark St, Urbana, IL 61801

ABSTRACT

We address the problem of automated image alignment for 3D volume reconstruction from stacks of fluorescent confocal laser scanning microscope (CLSM) imagery acquired at multiple confocal depths, from a sequence of consecutive slides. We focus on automated image alignment based on centroid and area shape features by solving feature correspondence problem, also known as Procrustes problem, in highly deformable and ill-conditioned feature space. In result, we compare image alignment accuracy of a fully automated method with registration accuracy achieved by human subjects using a manual alignment method. Our work demonstrates significant benefits of automation for 3D volume reconstruction in terms of accuracy, consistency, and performance time. We also outline the limitations of fully automated and manual 3D volume reconstruction system.

Keywords: 3D volume reconstruction, registration, fluorescence confocal laser scanning microscopy (CLSM), Procrustes problem

1. INTRODUCTION

Manual 3D volume reconstruction from stacks of laser scanning confocal microscopy (CLSM) images obtained from the study of serial histological sections is time consuming process. Reconstruction is complicated by potentially significant variations in intensity and shape of corresponding structures, unpredictable and frequently inhomogeneous geometrical warping during specimen preparation, and an absence of internal fiduciary markers for alignment. Given this assumption, 3D volume reconstruction can be performed by a semi-automated method with improved accuracy in comparison to manual method[1]. However, a long-term goal in multiple application domains, including medicine, mineralogy, or surface material science, is to automate 3D volume reconstruction while achieving at least the accuracy of a human operator. Through automation, it may be possible to save time and to achieve consistency in 3D reconstructions not possible with human-assisted reconstruction methods.

We developed methods to fully automate the 3D volume reconstruction of blood vessels and vasculogenic mimicry patterns in uveal melanoma from serial fluorescent labeled paraffin sections labeled with antibodies to CD34 and laminin and studied by confocal laser scanning microscopy. In uveal melanomas and other tumors, the detection of looping patterns that stain positive with the periodic acid-Schiff (PAS) in histological sections is associated with adverse outcome. These patterns, rich in laminin, are generated by highly invasive tumor cells and the patterns – although not blood vessels – conduct plasma outside of the conventional vascular microcirculation[2]. It is important to compare the 3D structure of these non-endothelial cell lined laminin-positive patterns with endothelial cell lined blood vessels in order to appreciate the flow of blood and plasma through these tumors.

The 3D reconstruction of vasculogenic mimicry patterns is a registration problem[3] requiring image pre- and post-processing steps to permit 3D visualization and quantification of these geometrical structures[4]. There is an abundance of registration technique and overview papers in the literature[5,6,7]. In the medical domain, several 3D volume reconstruction techniques have been developed based on specialized image acquisition procedures, e.g., using a linear differential transformer[8], or truncated pyramid representation[9].

The primary focus of this paper is on fully automating the reconstruction process by automatically establishing a correspondence between unlabeled segment features, and selecting an optimal subset of matched feature pairs, which is an extension of our previous work[1]. The overall process of automated 3D volume reconstruction follows: (1) detect registration features by segmenting out closed regions, e.g., vascular regions followed by computing features of segmented regions, e.g., centroids and areas, (2) establish correspondence of detected centroid features between adjacent

---

* pbajcsy@ncsa.uiuc.edu, phone: 217-265-5387, fax: 217-244-7396

slides, (3) select best subset of matched feature pairs, and (4) compute alignment transformation parameters and transform 3D sub-volumes into the final 3D volume.

2. HISTOLOGICAL MATERIALS

2.1. Material preparation

Formalin-fixed, paraffin-embedded uveal melanoma tissue samples were sectioned at 4 μm thickness. The use of archival human tissue in this study was approved by the Institutional Review Board of the University of Illinois at Chicago. Slides were deparaffinized in xylene and rehydrated through a decreasing ethanol gradient. Slides were rinsed in distilled water followed by antigen unmasking using Target Retrieval Solution 10X Concentrated (DAKO, Carpenteria, CA) according to the manufacturer's instructions and then rinsed in Phosphate Buffered Saline (PBS) for 5 minutes. Slides were incubated with monoclonal mouse anti-laminin antibody Sigma L8271, clone LAM 89 (Sigma, St. Louis, MO) at a dilution titer of 1:200 for 30 minutes at room temperature. Slides were rinsed in protein blocking solution (DAKO) for ten minutes followed by detection with Alexa Fluor 488 goat anti-mouse IgG (Molecular Probes, Eugene, OR) for 30 minutes at a dilution of 1:400. Slides were rinsed in buffer then mounted in Faramount Aqueous Mounting Medium (DAKO). For all staining procedures, secondary antibody was omitted in negative controls.

All histological serial sections were examined with a Leica SP2 laser scanning confocal microscope (Leica, Heidelberg, Germany) using the 40X objective. Images were stored in tagged information file format (TIFF). To reconstruct extravascular matrix patterns in primary human uveal melanoma tissue from 4 μm sections stained with laminin with signal detection by immunofluorescence as described above, we evaluated three 3D volumes experimentally. One 3D volume was formed from four consecutive sub-volumes consisting of 96 image frames, another one from six sub-volumes consisting of 48 image frames, and the third was formed from four sub-volumes consisting of 13 frames. Note that we have chosen visually the most salient image from each sub-volume for registration purpose, e.g., center frame.

2.2. Identifying internal features

It is difficult to align serial paraffin embedded using fiduciary markers artificially inserted into the tissues or blocks[10]. For example, the introduction of markers internally may distort tissue and its areas of interest. On the other hand, markers placed outside the tissue may migrate during sectioning or expansion of the paraffin. The structures of interest in this study – blood vessels and vasculogenic mimicry patterns – both contain laminin. In order to develop strategies for the automated alignment of tissue sections, we first aligned serial confocal laser scanning microscopy stacks of human tonsil tissue stained for laminin. The epithelial basement membrane of the tonsil is a highly irregular surface against which alignment algorithms can be developed. In addition, the tonsil stroma contains blood vessels which can be used to align tissue sections according to strategies described below. Thus, laminin-positive structures function as internal fiduciary markers in this study.

Based on the material preparation and laminin-positive structures function imaged by fluorescent CLSM, the automated 3D reconstruction process is based on the following two assumptions. First, at least one frame from each 3D sub-volume contains a set of closed or partially opened visually salient contours representing laminin-positive structures (presence of registration features). Second, certain shape characteristics of these salient contours, e.g., centroid or area, remain invariant under translation and rotation transformations (shape invariance of registration features across two 4 μm sections).

3. AUTOMATED 3D VOLUME RECONSTRUCTION

3.1. Registration Feature Detection

For automated feature matching, we need to identify the most descriptive features that can be extracted from images. Ideally, these descriptive features include parameters describing each segment shape so that homologous segments can be identified in a pair of images.

Feature region segmentation: The goal of this step is to segment out structural features that could be matched in two selected image frames. A simple intensity thresholding followed by connectivity analysis[11] would lead to segments that are enclosed by fluorescent pixels above a threshold value. Nonetheless, it is not always the case that all pixels along a segment circumference are lit up above the threshold that separates background (no fluorescence) and foreground

(fluorescent signal) because of specimen preparation imperfections and limitations of fluorescent imaging. Disregarding partially open/closed contours of lit up pixels could lead to an insufficient number of segments necessary for computing registration transformation parameters.

We therefore performed a segmentation that labels regions with partially closed high intensity contours. The algorithm is based on connectivity analysis of a thresholded image with a disk of a finite diameter, as it is illustrated in Figure 1 (a). A disk is placed at every background pixel location that has not yet been labeled. A segment (region) is formed as a connected set of pixels covered by a disk while the disk moves within the fluorescent boundary. The diameter of a disk determines what contours would lead to a detected segment that represents closed contours with a few permissible gaps.
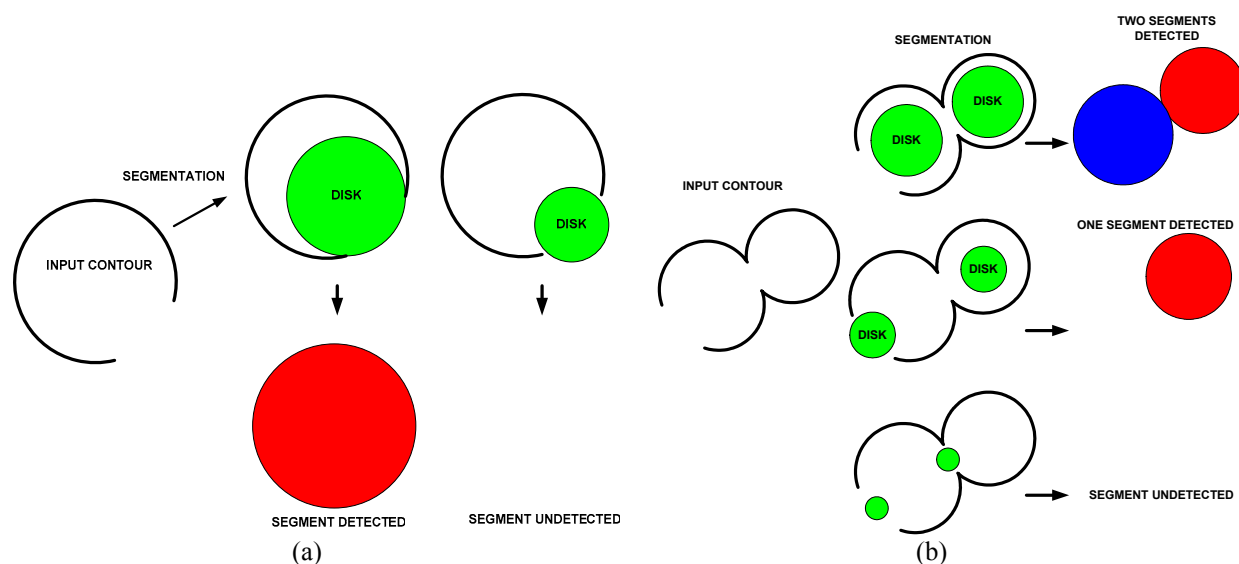

Figure 1: Illustration of disk-based segmentation: (a) a segment is formed as a connected set of pixels covered by a disk while the disk moves within the fluorescent boundary. (b) Depending on the disk diameter and contour gaps a segment is detected or not.

Figure 1 (b) shows multiple contour interpretations as a function of disk diameter resulting to a line or one closed contour or two touching contours. These interpretations are consistent with methods used by human investigators to select regions of interest from a partially closed contour.

In order to automate the segmentation process, the threshold value and disk diameter parameters must be chosen. The threshold value is usually based on the Signal-To-Noise (SNR) ratio of a specific instrument. It is possible to optimize the threshold value by analyzing the histogram of labeled region areas as a function of the threshold value because a large number of small areas (occurring due to speckle noise) disappear at certain range of threshold values. The choice of disk diameter for connectivity analysis is much harder to automate because it ties to the medical meaning of each closed or partially closed contour that would be selected by an expert. We automated the choice of a disk diameter by imposing lower and upper bounds on the number of segmented regions and evaluating multiple segmentation outcomes.

Feature Extraction: Based on our choice of the image transformation model for finding segment correspondences that consist of rotation and translation, we selected segment centroids and areas as the primary shape features. It is known that the segment areas, as well as the mutual distances between any two centroids of segments, are invariant under rotation and translation. Thus, we utilized the invariance of these two shape features during feature matching and registration parameter estimation. Both of the selected segment features were extracted after performing a connectivity analysis by simple pixel count (areas) and average (centroid) operations.

3.2. Feature Matching

We established an automated correspondence between two sets of segment features. The problem is a variant of the Procrustes problem[12], where one estimates transformation parameters based on centroid and area characteristics of

segments (segment feature). Our developed solution to the correspondence problem consisted of two phases. First, we estimated a coarse rigid transformation by (a) matching Euclidian distances between pairs of centroids (denoted as distance-based matching) and (b) comparing segment areas. Although this type of correspondence estimation is robust to partial mismatches, it is insensitive to angular differences (see Figure 2). Second, we rotated and translated segments from the set T to the coordinate system of the set S according to the parameters computed in the first phase, as shown in Figure 3. Finally, we found correspondences by matching vector distances, as opposed to Euclidean distances used in the first phase (denoted as vector-based matching). This computation is appropriate for correcting wrong correspondences from the first phase, but would not be robust on its own for highly rotated segments.
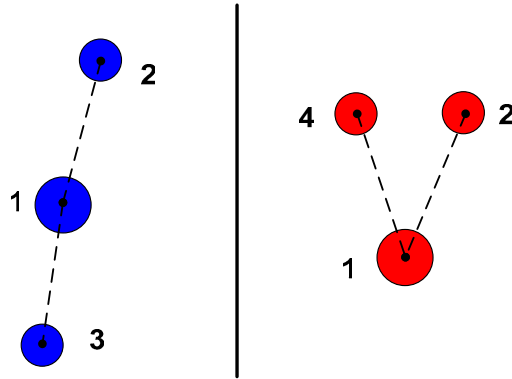

Figure 2: Illustrations of the case when distance-based matching leads to an erroneous match of the segments labeled as 3 (left) and as 4 (right).

The developed solution to the correspondence is presented here. Let us suppose that we extracted two sets of shape features $S_a (a = 1, ..., N^S)$ and $T_b (b = 1, .., N^T)$ from two selected image frames I_a^S and I_b^T such as $S_i = \{\vec{c}_i^S, a_i^S\}$ and $T_j = \{\vec{c}_j^T, a_j^T\}$, where $\vec{c}_k^\Omega$ are the 2D centroid locations and a_k^Ω are the area values. The number of features in each image is N^Ω, $\Omega = \{S, T\}$, and N^S is not necessarily the equals to N^T. An illustration of the correspondence problem is presented in Figure 3 for $N^S = 3$ and $N^T = 5$.
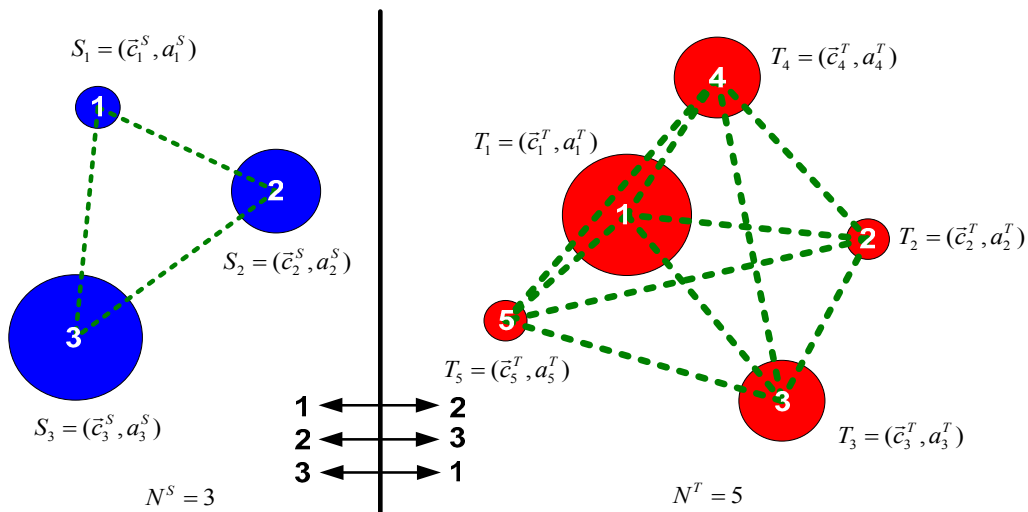

Figure 3: Illustration of the correspondence problem for two sets of features S_i and T_j with unequal number of features $N^S = 3$ (left) and $N^T = 5$ (right). Segments are shown as disks characterized by their index i, area a_i^S and centroid location $\vec{c}_i^S$. Dashed lines represent the Euclidean distances between any two centroid locations.

SPIE USE: _____ DB Check, _____ Prod Check, Notes:

In the first phase, the computation consists of (1) calculating a matrix of mutual distances d_{iu}^S and d_{jv}^T ($i, u = 1, ..., N^S$ and $j, v = 1, ..., N^T$) for each set of segment centroids (e.g., dotted lines in Figure 3), (2) finding a set of matching pairs of segments M_k, and (3) sorting the matched segments based on the residuals of all matched centroids with respect to the estimated rigid transformation. To find a matching pair of segments, we first select a pair of segments S_i and T_j denoted by pivot segments, and introduce three similarity measures, such as (a) the area ratio $A_{ij}(u, v)$, (b) the difference of Euclidian distances (residual) $D_{ij}(u, v)$, and (c) the number of matching segments Q_{ij}.

Pivoted by segments (S_i, T_j), we first compute the area ratio as $A_{ij}(u, v) = \left| a_u^S / a_v^T - 1 \right|$ for matching segments (S_u, T_v). Next, the difference of Euclidian distance is computed as $D_{ij}(u, v) = \left| d_{iu}^S - d_{jv}^T \right|$. Finally, the number of matching pairs Q_{ij} is calculated by counting the number of pairs that satisfies both $D_{ij}(u, v) < \delta_1$ and $A_{ij}(u, v) < \varepsilon_1$, where the value of δ_1 is the dissimilarity upper bound of a pair of distances, and ε_1 is the divergence upper bound of a ratio of two segment areas from one. We not only maximize Q_{ij} but also remove the matches that do not satisfy the inequality $\dfrac{Q_{ij}}{\mathrm{Min}(N^S, N^T)} \geq \lambda_1$, where $\lambda_1 \in [0,1]$ is the lower bound of normalized number of matches for a single pivot segment. Figure 4 shows the description of the defined similarity metrics.
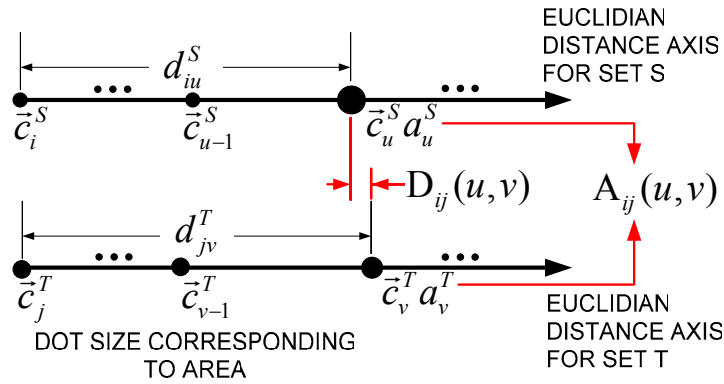

Figure 4: Illustration of distance-based matching for two pivot segments $S_i = \{\vec{c}_i^S, a_i^S\}$ and $T_j = \{\vec{c}_j^T, a_j^T\}$. In order to find the best match, distance and area ratio of pairs of segments are compared to satisfy $D_{ij}(u, v) < \delta_1$ and $A_{ij}(u, v) < \varepsilon_1$.

To find a final match M_k, we maximize a score function $f(\cdot)$ by incorporating three similarity metrics as follows:

$$M_k = \left\{ (i, j) \middle| (i, j) = \arg\max_{i,j} \left\{ f\left(Q_{ij}, \frac{1}{\overline{D}_{ij}}, \overline{A}_{ij} \right) \right\} \right\} \qquad (1)$$

where $\overline{D}_{ij}$ and $\overline{A}_{ij}$ are average error distance and area ratio pivoted by (S_i, T_j) for all matching pairs of (u, v), $0 \leq k \leq N^{ST}$, and N^{ST} is the number of matching pairs of segments (pivots). The function $f(\cdot)$ may be defined as an energy function or, more simply, a weighted product of all components. In our implementation, we used a weighted product of each component with normalization.

In the second phase, we first rotated segments from the set $T_b (b = 1,.., N^T)$ to the coordinate system of the set $S_a (a = 1,..., N^S)$ according to the parameters which is computed by selecting two best matches in the first phase. Next, vector-based matching is performed in a similar way as distance-based matching in the first phase. The major difference is in replacing the Euclidian distance metric $D_{ij}(u,v)$ with the vector distance metric $D^*_{ij}(u,v)$ defined in Equation (2).

$$D^*_{ij}(u,v) = \left\| (\vec{c}^S_i - \vec{c}^S_u) - (\vec{c}^T_j - \vec{c}^T_v) \right\| \tag{2}$$

According to the distance metric in the Equation (2), the vector distance incorporates both Euclidian distance and angular constrains about a pivot segment. Therefore, the matching performance is greatly increased comparing with the first phase in terms of accuracy (mismatch) and the number of matching segments. The second phase contains the same three parameters as the first phase, and we denoted them as ε_2, δ_2 and λ_2. In almost all experimental cases, we have set $\varepsilon_1 = \varepsilon_2$, $\delta_1 = \delta_2$ and $\lambda_1 = \lambda_2$.

3.3. Image Transformation and Selection of Feature Pairs

Based on the material preparation procedure and the assumptions of developed correspondence problem approach, the affine transformation model is constrained to only small amounts of scale and shear deformations. Therefore, we selected an affine transformation model for the final image transformation.

From the image alignment accuracy viewpoint, selected pairs of segment centroids should be well spatially distributed in each image and should not be collinear. If points are close to be collinear then the affine transformation parameters cannot be uniquely derived from a set of linear equations (more unknowns than the number of equations), which leads to large alignment errors. If points are locally clustered and do not cover an entire image spatially then the affine transformation is very accurate only in the proximity of the selected points. However, the affine transformation inaccuracy increases with the distance from the selected points, which leads to large alignment errors because a registration error metric takes into account errors across the entire image area. In order to assess the pairs of matched centroid points in terms of their distribution and collinear arrangement, we have designed a compactness measure. It is defined as a ratio of the entire image area divided by the largest triangular area formed from the points as described in our previous work[1]. The measure is defined mathematically in Equation (3).

$$Compactness\ Measure = \frac{Area_{IMAGE}}{Area_{TRIANGLE}} \tag{3}$$

3.4. Evaluations of Image Alignment Accuracy

Our primary evaluation criterion of image alignment is its registration accuracy. We compare image alignment accuracy of the proposed fully automated method with registration accuracy achieved by human subjects using a manual registration method. There are three fundamental questions that arise during registration accuracy evaluations, such as (1) what to compare any registered image with, and (2) how to compare multiple image alignment results, and (3) how to evaluate accuracy of alignment (the choice of metrics).

Evaluation images: Figure 5 shows three pairs of misaligned images with known deformations by taking the first and last images along the z-axis within one CLSM stack (co-registered sub-volume). The pairs of images are created by applying a representative affine transformation $\alpha^{GT}(\cdot)$ to the last image with known transformation parameters as the same way in our previous work[1]. The representative affine transformation was determined from a set of all affine transformations obtained during manual 3D volume reconstructions. The last image before transformation is the ground truth image with respect to which both manual and automatic reconstructions are compared. All pixel coordinates of the transformed (ground truth) image $\mathbf{P}^{GT} = \{p^{gt}_1, p^{gt}_2, ..., p^{gt}_n\}$ are defined by the affine transformation $\alpha^{GT} : p_i \rightarrow p^{gt}_i$ for every pixel location $\mathbf{P} = \{p_1, p_2, ..., p_n\}$.
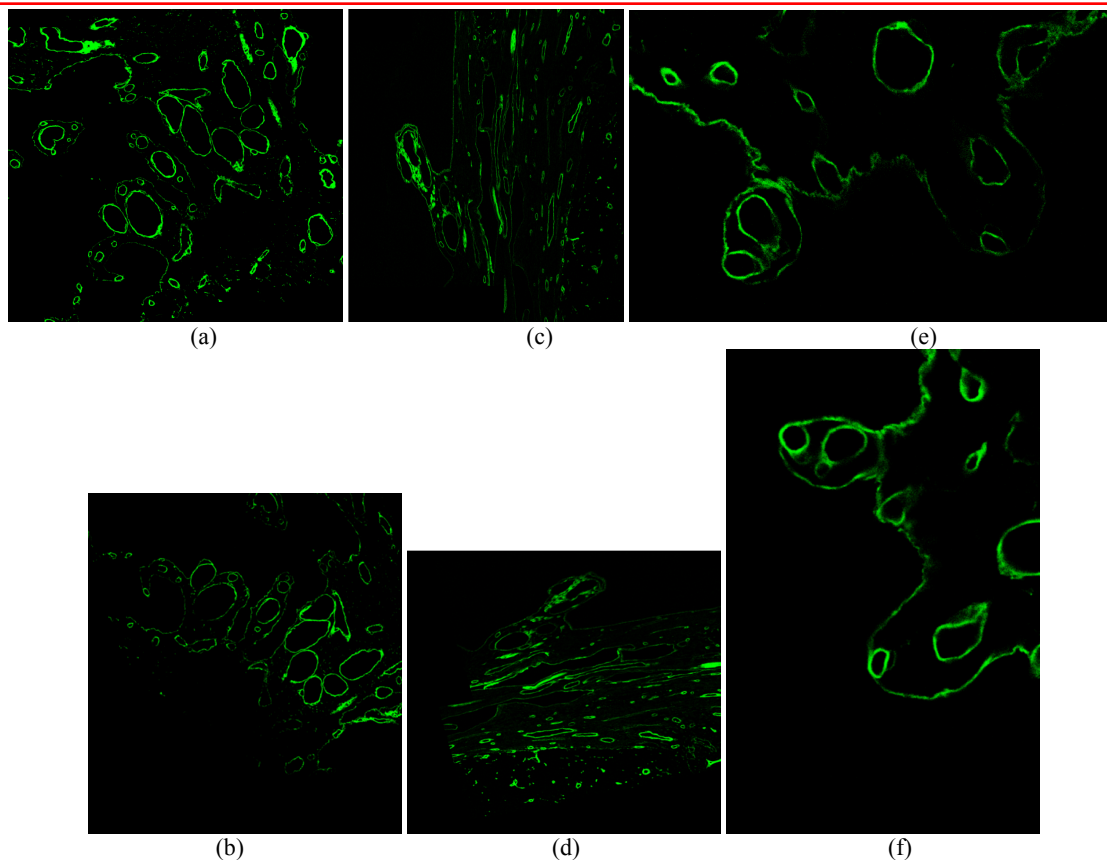
Figure 5: Three selected pairs of evaluation images ((a)-(b), (c)-(d), and (e)-(f)): Note that images (b), (d), and (f) are rotated by 90 degrees from the original acquisition to demonstrate the robustness of the automated feature matching.

Registration software: The evaluation images are presented to a human subject or to an image alignment algorithm. For the manual registration, the human-computer interface (HCI) for selecting points or segments is identical to our web-enabled interface at http://isda.ncsa.uiuc.edu/MedVolume.

Evaluation metric: We chose to compare multiple alignment results by computing an average distance between a ground truth location and a location obtained from user defined transformation[1]. The average distance E becomes our evaluation metric and is calculated over all image pixels according to Equation (4)

$$E = \frac{1}{n}\sum_{i=1}^{n}\sqrt{(p_{ix}^{gt} - p_{ix}^{usr})^2 + (p_{iy}^{gt} - p_{iy}^{usr})^2} \quad\quad (4)$$

where n is the number of transformed image pixels, and $\mathbf{P}^{USR} = \{p_1^{usr}, p_2^{usr}, ..., p_n^{usr}\}$ are the transformed pixel coordinates according to the estimated affine transformation $\alpha^{USR} : p_i \rightarrow p_i^{usr}$ by user point selections. The set of affine parameters is obtained from manual (human subject's point selection and matching) or fully automated registration methods.

4. RESULTS

4.1. Manual Alignment Results

The experimental data consist of the total of 102 manual alignment trials with twenty human subjects. The compactness measure developed for automated alignment method (see Equation (3)) was applied to the set of points selected by

human subjects, and the compactness measure values for all alignment trials are shown in Figure 6. In order to eliminate the worst results, statistical analysis was applied. The elimination was based on a threshold value equal to 99.73% statistical confidence interval from the average and standard deviation values of all compactness measures (set to 1162.16). Figure 6 shows an alignment error as a function of the corresponding compactness measure reported for all experiments. Table 1 summarizes results statistically per image pair.
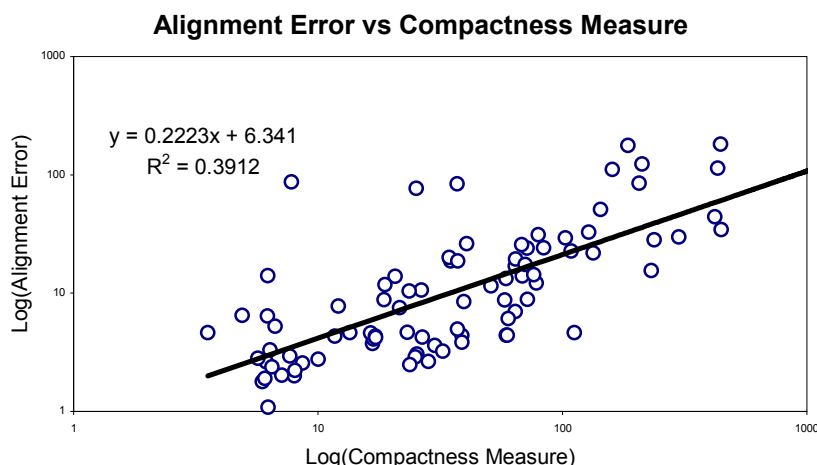

Figure 6: This graph illustrates alignment error as a function of compactness measure associated with each trial. A large value of compactness measure implies that the control points selected during manual alignment are spatially dense or close to being collinear, thus leading to large alignment error. A hypothetical linear relationship of the variables is shown.

Table 1: A summary of manual image alignment experiments for 99.73% confidence interval. The table provides statistics computed from 86 human alignment trials after eliminating the worst 6 trials.

Error [pixels] Confidence Interval = 9.73% (Compactness measure threshold =1162.16)	Manual (Pixel-Based)			
	Image pair 1	Image pair 2	Image pair 3	All Images
Average	43.57	22.42	21.49	29.22
Standard Deviation	77.11	33.95	36.34	53.38

4.2. Automated Alignment Results

Table 2 contains results obtained using automated alignment. The automated alignment leads to the same result every time the algorithm is executed with the same data therefore the standard deviation is equal to zero for each image pair and equal to 2.07 and 0.47 over all three image pairs. The results of segmentation are shown in Figure 7 (original) and Figure 8 (segmentation) following the segmentation method described in the previous Section. Figure 9 illustrates the correspondences found for the segments shown in Figure 8 by considering centroid and area segment features. In Figure 10, the circles denote three pairs of centroid points that were selected from the set of all pairs shown in Figure 9 according to the proposed compactness measure defined in Equation (3).

Table 2: A summary of automatic image alignment experiments.

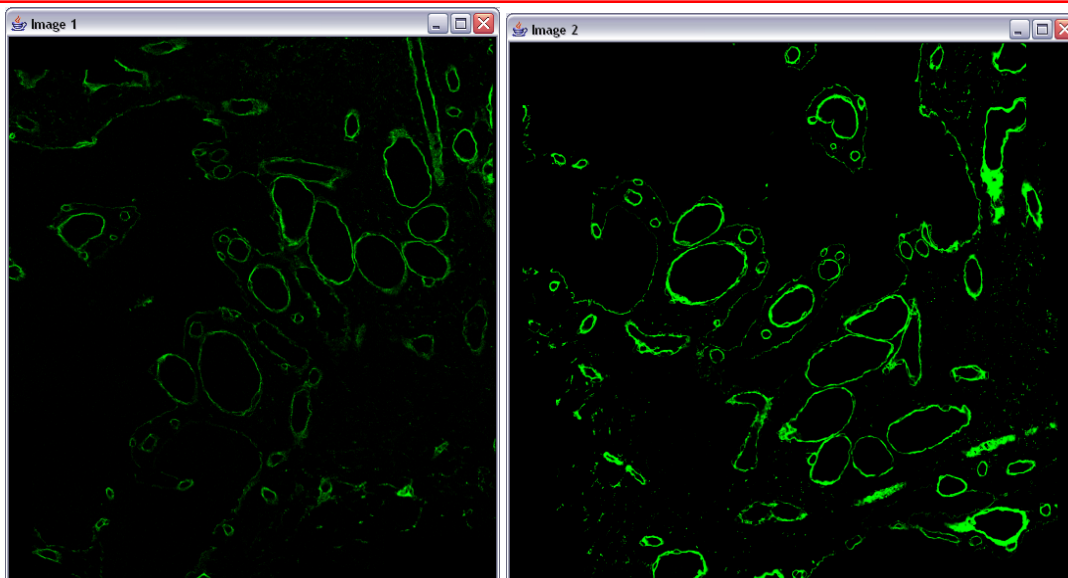| Error [pixels]	Automatic (feature based)			
	Image pair 1	Image pair 2	Image pair 3	Average
Average	1.2839	2.6508	5.3500	3.0949
Standard Deviation	0	0	0	2.0691

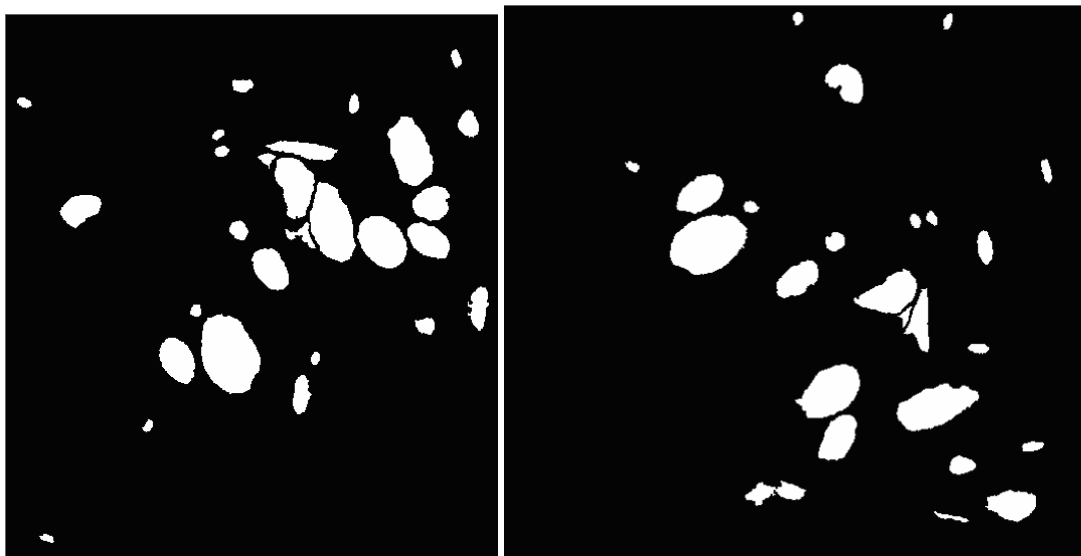Figure 7: A pair of example images that have to be aligned.

Figure 8: Segmentation of input images shown in Figure 7. Segmentation is performed by thresholding that is followed by connectivity analysis with a disk. The two images illustrate results obtained with different disk parameters [Left image – T.S. (threshold S) = 10, right image – T.T. (threshold T) = 8, M.R. (minimum size of a region) = 80, and D.D. (disk diameter) = 1].
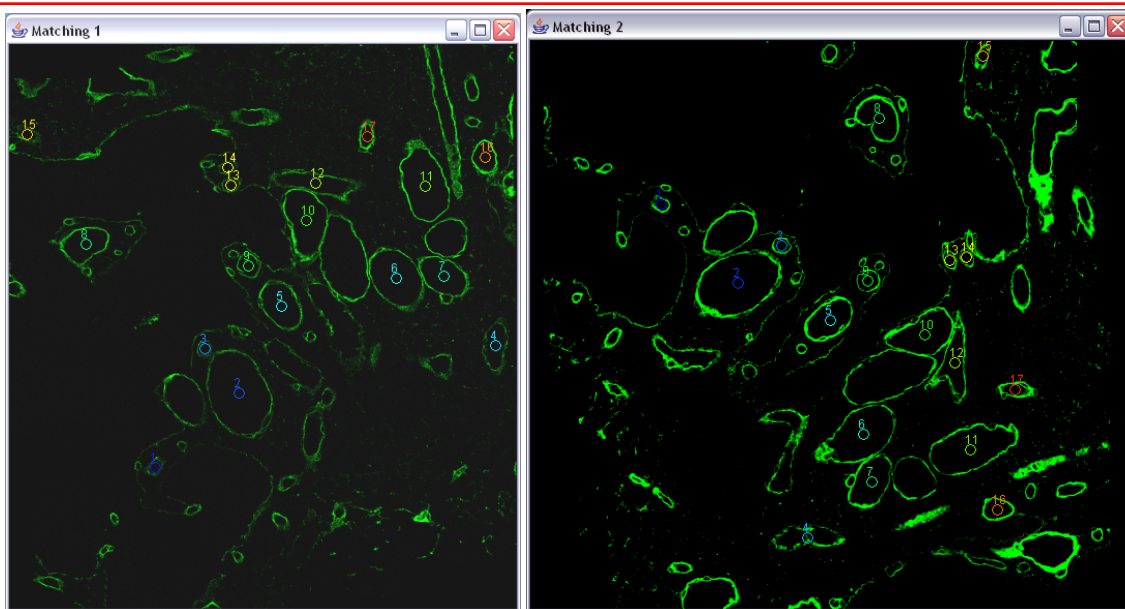
Figure 9: The correspondence outcome from two phases for the segments shown in Figure 8. The left and right images are to be aligned. Overlays illustrate established correspondences between segments that are labeled from 1 through 17. The centroid locations of segments are sorted based on the correspondence error from the smallest error to the largest error.
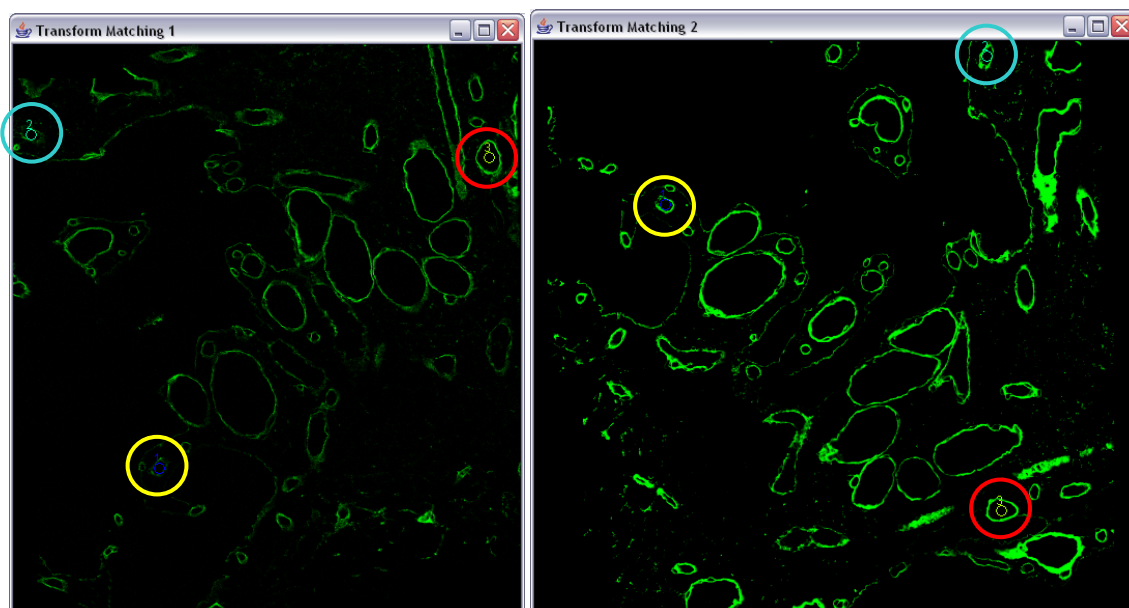

Figure 10: The result of automated feature selection for the original images shown in Figure 8 after they were processed to establish segment correspondences shown in Figure 9. The circles of different colors represent three pairs of centroids selected automatically according to the compactness measure defined in Equation (3).

The algorithmic parameters selected for the three evaluation pairs of images are shown in Table 3. The set of parameters includes (1) threshold values for images S and T, disk diameter, and minimum acceptable segment size in the segmentation step, and (2) limiting values for centroid distances ($\varepsilon_1, \varepsilon_2$), segment areas ($\delta_1, \delta_2$), and numbers of segment matches (λ_1, λ_2) in the matching step. Ideally, one would like to perform general optimization of all parameters. In our case instead, the problem was constrained (1) to the same imaging device but acquiring data over a time period of

several months, and (2) to the same class of specimens but prepared in separate batches. The parameters shown in Table 3 illustrate the small variability of parameter values.

Table 3: Manually selected parameters of the proposed 3D volume reconstruction method for the three evaluation pairs of images (T.S: threshold of image S, T.T: threshold of image T, M.R: minimum region size for valid features, D.D: disk diameter, ε : divergence of upper bound of ratio of two matching segment areas from one, δ : dissimilarity upper bound of a pair of distances, λ : lower bound on the number of normalized matches.)

Image	Phase	T.A (value)	T.B (value)	M.R (pixel)	D.D (pixel)	ε (ratio)	δ (pixel)	λ (ratio)
1	1	1	1	50	2	1.2	20	0.4
	2	1	1	50	2	1.5	20	0.4
2	1	20	20	50	3	1.5	20	0.4
	2	20	20	50	3	1.5	20	0.4
3	1	20	20	50	3	1.5	15	0.4
	2	20	20	50	3	1.5	20	0.4

5. CONCLUSIONS

We presented a solution to 3D volume reconstruction of blood vessels and vasculogenic mimicry patterns in histological sections of uveal melanoma from serial fluorescent labeled paraffin sections labeled with antibodies to CD34 and laminin and studied by CLSM. Our work demonstrates significant benefits of automation for 3D volume reconstruction in terms of achieved accuracy (on average, 9.4 or 15 times smaller alignment), consistency (25.8 or 113.7 times smaller standard deviation) of results and performance time. We also outlined the limitations of fully automated and manual 3D volume reconstruction systems, and described related automation challenges. We have tried to show that given computational resources and repetitive experimental data, the automated alignment provides more accurate and consistent results than a manual alignment approach. With the proposed approach, the automation will reduce the alignment execution time and cost in the future, as the cost of more powerful computers goes continuously down.

To our knowledge, there have not been developed robust and accurate fully automated 3D volume reconstruction methods from a stack of CLSM images without artificially inserted fiduciary markers. Our research work is also unique in terms of forming a complete system for medical inspection of 3D volumes reconstructed from CLSM images. Our approach to automating the reconstruction process incorporates the tradeoffs between computational requirements and uncertainty of resulting reconstructions introduced by each processing step. For example, just to perform alignment refinement over a small pixel neighborhood requires significant computational resources[13]. Thus, the approach based on morphology-based alignment followed by intensity-based refinement accommodates our prior knowledge about data and limitations of our computational resources. The contribution of this paper is in the presentation and development of fully automating the 3D reconstruction by automatically establishing feature correspondences between unlabeled segment features, and selecting an optimal subset of matched feature pairs for optimal transformation parameter estimation. In our experimental results, we presented the accuracy evaluation for manual and fully automated 3D volume reconstruction technique.

The limitations of the fully automated 3D reconstruction system came from all modeling assumptions, such as (a) the presence of partially closed contours of fluorescent pixels, (b) shape invariance along z-axis for two depth adjacent sub-volumes, (c) satisfactory signal-to-noise ratio (SNR), (d) limited amount of scale and shear deformations due to specimen preparation and imaging, and (e) sufficient number of detected features (at least three pairs). In addition, selection of algorithmic parameters pose still challenges for automation although the algorithmic parameters in Table 3 demonstrated a very negligible change from image to image. The limitations of the manual 3D volume reconstruction are clearly consistency, the cost of human time needed to perform image alignment, and knowledge requirements to achieve good alignment accuracy (e.g., the time for training human subjects). In general, the time spent on each 3D volume reconstruction task is non-linearly proportional to the resulting quality with certain insurmountable quality limits.

ACKNOWLEDGEMENT

REFERENCES

1. S-C. Lee and P. Bajcsy, "Feature based registration of fluorescent LSCM imagery using region centroids*." Proc. SPIE* 5747, 170-181, 2005.
2. R. Folberg and A. Maniotis, "Vasculogenic mimicry." *APMIS* 112, 508-525, 2004.
3. J. Maintz and M. Viergever, "A survey of medical image registration." *Med. Image Anal.*, 2, 1-36.
4. J. Wu, B. Rajwa, D. Filmer, C, Hoffmann, B. Yuan, C. Chiang, J. Sturgis and J. Robinson "Automated quantification and reconstruction of collagen matrix from 3D confocal datasets." *J. Microsc.* 210, 158-165, 2003.
5. D. Hill, P. Batchelor, M. Holden and D. Hawkes, "Medical image registration." *Phys. Med. Biol.* 46, R1-R45, 2001.
6. L. Brown, "A survey of image registration techniques." *ACM Comp. Surveys* 24, 326-276, 1992.
7. B. Zitova and J. Flusser, "Image registration methods: A survey." *Image Vis. Comp.* 21, 977-1000, 2003.
8. J. Alkemper and P. Voorhees, "Quantitative serial sectioning analysis." *J. Microsc.* 201, 388-394, 2001.
9. C. Papadimitriou, C. Yapijakis and P. Davaki, "Use of truncated pyramid representation methodology in three-dimensional reconstruction: an example." *J. Microsc.* 214, 70-75, 2004.
10. J. Spacek, "Three-dimensional reconstructions of astroglia and oligodendroglia cells." *Z. Zellforsch. Mikroskop, Anat.* 112, 430-442, 1971.
11. R. Duda, P. Hart and D. Stork, Pattern classification (Second Edition), 654, *Wiley-Interscience*, New York, N.Y, 2001.
12. L. Dorst, "First order error propagation of the procrustes method for 3D attitude estimation." *IEEE Trans. Pattern Anal. Mach. Intell.* 27, 221- 229, 2005.
13. R. Kooper, A. Shirk, S-C. Lee, A. Lin, R. Folberg and P. Bajcsy, "3D volume reconstruction using web services." *Proc. IEEE Int. Conf. Web Services* 2, 709-716, 2005.

SPIE USE: _____ DB Check, _____ Prod Check, Notes: